Effect of Residual Gas Composition on Epitaxial Growth of Graphene on SiC

J. Kunc,* M. Rejhon, E. Belas, V. Dědič, P. Moravec, and J. Franc
Institute of Physics, Faculty of Mathematics and Physics, Charles University in Prague, Ke Karlovu 5, CZ-121 16 Prague 2, Czech Republic

(Received 10 January 2017; revised manuscript received 25 August 2017; published 23 October 2017)

In recent years, graphene growth optimization has been one of the key routes towards large-scale, high-quality graphene production. We measure *in situ* residual gas content during epitaxial-graphene growth on silicon carbide (SiC) to find detrimental factors of epitaxial-graphene growth. The growth conditions in high vacuum, in argon, purified argon, and the flow of argon are compared. The grown epitaxial graphene is studied by Raman-scattering mapping. We determine mechanical strain, number of graphene layers and the graphene quality. The surface topography is measured by atomic force microscopy. Charge density and carrier mobility are studied by Hall-effect measurements in van der Pauw configuration. We identify the major role of the chemical reaction of carbon and residual water. The rate of the reaction is lowered when purified argon is used. We also show that, according to time-varying gas content, it is preferable to grow graphene at higher temperatures and shorter times. Other sources of growth environment contamination are also discussed. The reaction of residual gas and SiC is discussed as one of the factors decreasing the lateral size of SiC atomically flat terraces and leading to their irregular shape. The importance of purified argon and its sufficient flow rate is concluded to be important for high-quality graphene growth as it reduces the rate of undesired chemical reactions and provides a more stable and defined growth ambient.

DOI: 10.1103/PhysRevApplied.8.044011

I. INTRODUCTION

Epitaxial-graphene growth on SiC [1] is a scalable fabrication method of high-quality graphene for postsilicon electronics and optoelectronics [2,3]. Among alternative devices, the growth technique, together with SiC wafer preparation, stands at the beginning of the whole manufacturing process. It is, therefore, a key to understanding the conditions under which reproducible high-quality graphene can be reached [4,5]. The growth mechanisms have been studied both theoretically and experimentally. First-principles calculations have been done to study graphene buffer-layer formation on SiC(0001), the diffusion of carbon on SiC [6], and the stability and reactivity of atomic steps of SiC in the initial graphene growth stage [7]. Experimental studies have been done to understand the mechanisms of epitaxial-graphene growth on SiC$(000\bar{1})$ [8], SiC(0001) [9], and nonpolar SiC surfaces [10], and to elucidate the roles of carbon diffusion [11] and silicon sublimation [9].

It has been shown that graphene with a reduced pit density can be grown on nominally flat SiC substrates [9] and graphene quality can be further improved when grown amid high argon pressure [12]. On the other hand, the carrier mobility has been observed to decrease with increasing argon pressure when time and temperature are kept constant [12]. Other strategies to improve graphene quality involve thermal decomposition of deposited polymer adsorbate, which acts as a carbon source [13]. The SiC step bunching, another issue reducing carrier mobility in epitaxial graphene on SiC, has been solved by amorphous carbon step pinning [14]. The thermodynamics of stable phases that governs the onset of graphene formation [5], oxidation [15], and other chemical reactions [16] has been discussed, too. However, there is little to no experimental evidence of graphene growth conditions and composition of a residual gas inside a graphene furnace [17]. These studies are restricted to gas-phase dynamics during chemical-vapor-deposition graphene growth [18] and to carbon-nanotube growth [19].

Here, we determine experimentally the residual gas content in a furnace for epitaxial-graphene growth on SiC. The measurements are performed *in situ* by a residual gas analyzer during the entire graphene growth. We show that the initial graphene growth is accompanied by chemical reaction of residual water and carbon. We compare the chemistry of graphene growth in high vacuum and at low argon pressure.

The comparison of both growth techniques demonstrates that argon reduces the rate of water and carbon reaction. Therefore, the amount of residual gas is smaller and the graphene quality is higher. We discuss also the role of argon in terms of growth temperature, time, gas purity, and gas flow. The graphene quality is analyzed by Raman-spectroscopy mapping, atomic force microscopy (AFM) and by Hall-effect measurements. We compare the growth in vacuum and in high-pressure argon in terms of strain, strain lateral

*kunc@karlov.mff.cuni.cz

 © 2017 American Physical Society

distribution, size of the SiC crystallographic terraces, and carrier mobility.

II. SAMPLES AND EXPERIMENTAL SETUP

The wafers of 4*H*-SiC were purchased from II-VI Inc. and are diced into 3.5×3.5 mm^2 rectangles. The samples are (500 ± 25) μm thick and we use semi-insulating, high-resistivity (10^{10} Ω cm) vanadium-doped SiC. Graphene is grown on the silicon face SiC(0001) with a wafer miscut of $\pm 0.6°$. The wafers are chemically mechanically polished and the surface roughness is about 0.5 nm. Diced samples are rinsed and sonicated in acetone and isopropyl alcohol for 10 min. The semi-insulating samples are heated in a graphite crucible by radio-frequency (rf) induction heating at 250–270 kHz. The graphite used for fabrication of the crucible is isostatically pressed (ISP) graphite and glassy (vitreous) graphite. The ISP graphite has the density 1850 kg/m^3 and the electrical resistivity 11×10^{-4} Ω cm. The glassy graphite, purchased from Final Advanced Materials, is used as a reference to study effect of crucible prebaking. High epitaxial-graphene quality was achieved with the confinement-controlled-sublimation (CCS) technique [20]. The processing environment is either high-vacuum 5×10^{-6} mbar or high-purity argon (a 6*N*-purity gas vessel).

The argon is further purified to the level of 9*N* purity by gas purifiers to remove residual oxygen and water. The stainless-steel gas tubes are outgassed at a temperature of about 200°C for 2 h prior to graphene growth to avoid contamination by residual water and impurities from the stainless-steel surface. The temperature is monitored by either a type-*C* thermocouple or a two-color pyrometer working at 0.95- and 1.05-μm wavelengths. The pyrometer allows us to measure the temperature with a spatial resolution of about 0.2 mm. The thermocouple of type *C* is electrically isolated by alumina shielding. The graphite crucible is placed inside a hot-wall reactor made of a 4-mm-thick and 250-mm-long quartz tube. The quartz tube is opened from both sides to allow effective gas circulation. The growth environment is studied with a residual gas analyzer (Prisma Plus QMG 220).

CF-40 flanges are used for all connections, except that of the adapter between the furnace and the turbomolecular-pump and quartz-tube feedthrough. The quartz feedthrough is made of two O rings on both sides to allow for a leak-tight connection up to high vacuum, 1.5×10^{-6} mbar, and yet allowing easy access to the reaction chamber.

III. TEMPERATURE MEASUREMENTS

The standard furnace design for epitaxial-graphene growth uses either a thermocouple or a pyrometer to monitor the growth temperature. We use both methods and compare them. The thermocouple is a cheaper method and it measures temperature inside the graphite crucible. It requires electrical isolation (made of alumina for high-temperature purposes up to 2000 °C), complicating furnace design and introducing other elements besides carbon and silicon (a SiC sample and a C-based crucible). We find that the electrical shield made of alumina (polycrystalline Al_2O_3) is sputtered and deposited on a relatively colder quartz tube during the cooldown process. Energy-dispersive x-ray spectroscopy is performed to determine the chemical composition of the sputtered material, as shown in Fig. 1 for three different positions along the inner part of the quartz tube. We find the presence of an aluminum and Al_2O_3 mixture. Their relative ratio changes along the quartz tube.

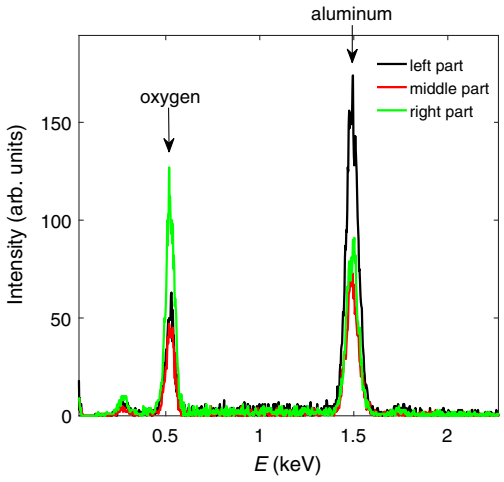

FIG. 1. Energy-dispersive x-ray analysis of a quartz tube coated during the thermocouple-monitored growth process. The aluminum-oxygen mixture with a varying content of aluminum is observed along the quartz tube.

As we use thermocouple type *C*, which is composed of rhenium and tungsten, we look carefully for traces of those metals as well. The negative result of our search leads us to conclude that the sputtered alumina from the thermocouple electrical shield is a source of furnace contamination, very often seen in high-temperature graphene furnaces. We expect the alumina traces to also contaminate the SiC wafer and the graphene. Hence, in order to keep high graphene quality, we propose using only remote temperature sensing with a pyrometer. We also note that it is essential to use a two-color ratio pyrometer to avoid temperature misreading due to the possible contamination of the furnace quartz windows. Contamination leads to a decreased light intensity and to the lower effective temperature determined by a one-color pyrometer.

IV. GRAPHITE CRUCIBLE

We study here the effect of gas adsorption in a graphite crucible. The commonly used ISP graphite and glassy graphite crucibles are compared. The major issue with ISP graphite is its high porosity and its permeability to gases. The high permeability leads to undesired contamination by air when the samples are exchanged or the graphite crucible is stored at ambient conditions for a longer time (on the

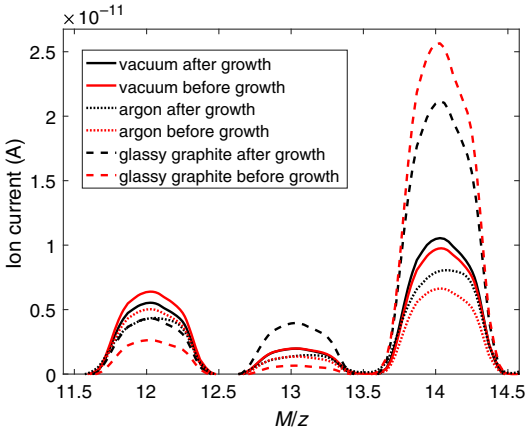

FIG. 2. Mass spectra with an M/z ratio ranging from 12 to 14. The residual gas spectra measured in the furnace before (the red solid, dashed, and dotted lines) and after (the black solid, dashed, and dotted lines) graphene growth at 1550 °C for 30 min. The prebaking at 800 °C for 10 min and at 1000 °C for 10 min is performed prior to graphene growth. The growth atmosphere is studied for the case of high vacuum at 5×10^{-6} mbar using a graphite crucible (the solid lines), low-pressure 9N-purity argon at 5×10^{-6} mbar (the dotted lines), and, at high vacuum of $5 \times 10^{-5} - 10^{-4}$ mbar using an unbaked glassy graphite crucible (the dashed lines). The base pressure is 1.5×10^{-6} mbar prior to rf heating in all cases.

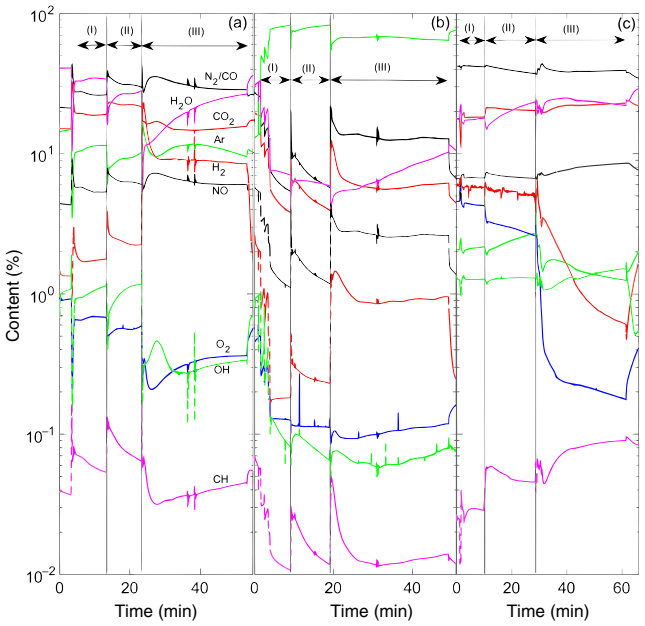

FIG. 3. Residual gas composition during graphene growth at high vacuum of 5×10^{-6} mbar using (a) graphite crucible, (b) low-pressure 9N-purity argon at 5×10^{-6} mbar and at high vacuum of $5 \times 10^{-5} - 10^{-4}$ mbar using (c) an unbaked glassy graphite crucible. The three growth stages are marked as follows: (I) preannealing at 800 °C for 10 min, (II) preannealing at 1000 °C for 10 min, and (III) graphene growth at 1550 °C for 30 min. Temporal evolution is shown for the major growth environment components; nitrogen or carbon monoxide (the black solid line), carbon dioxide (the red solid line), argon (the green solid line), oxygen (the blue solid line), water (the magenta solid line), nitrogen monoxide (the black dashed line), hydrogen (the red dashed line), a −OH fragment (the green dashed line), and a −CH fragment (the magenta dashed line).

order of hours or longer). A glassy graphite is impermeable to gases; hence, it is more convenient to keep the furnace environment clear of air residual gases. The residual gas stored in ISP graphite is removed within the first two prebaked graphene growth stages. The pressure usually grows from 1.5×10^{-6} mbar to 1.5×10^{-3} mbar or more if the crucible is not well baked. The well-baked crucible exhibits a small rise of the residual gas pressure of less than 1 order of magnitude, typically 1.5×10^{-6} mbar to 1.5×10^{-5} mbar.

Unlike ISP graphite, glassy graphite is impermeable to gases, and the prebaking removes surface absorbants only. The glassy carbon crucible is less susceptible to long exposure to air; however, its prebaking at a temperature much higher than the growth temperature is also necessary, as shown in Fig. 2. The well-baked graphite crucible exhibits comparable strength of peaks at $M/z = 12$ (carbon) and 14 (nitrogen), which is also the signature of a leak-tight vacuum chamber. The unbaked glassy graphite exhibits more than the 2×-stronger nitrogen peak which is supposed to come from a glassy graphite surface. We use a peak at $M/z = 14$ instead of $M/z = 28$ because the latter overlaps with carbon monoxide.

V. GROWTH ATMOSPHERE

The general growth process consists of three stages. The prebaking stage (I), depicted in Fig. 3, is used for crucible outgassing at 800 °C for 10 min. The second prebaking stage (II), 1000 °C–1100 °C for 10 min, is used to decompose a native oxide layer on a SiC wafer. The graphene growth stage (III) is performed at temperatures of 1400 °C − 2000 °C at time periods ranging from minutes to hours. Figure 3 depicts the relative content of the growth ambient in all three growth stages for the case of growth in high vacuum [Fig. 3(a)] under continuous vacuum pumping by a turbomolecular pump, low pressure argon [Fig. 3(b)] under continuous pumping, and limited argon leaking and growth in high vacuum using a glassy graphite crucible [Fig. 3(c)]. The graphene growth stage (III) is limited to 30 min to show longtime evolution of the growth ambient.

A change of relative content is caused by a different pumping rate (e.g., slow hydrogen pumping), outgassing from the vacuum-chamber walls (mainly water), and chemical reactions. We identify that oxidizing reactions appear at every temperature rise [from step (I) to (II) and from step (II) to (III)], resulting in reductions of both the relative and the absolute amount of oxygen. These reactions are, however, negligible for the very small amount of oxygen in the chamber.

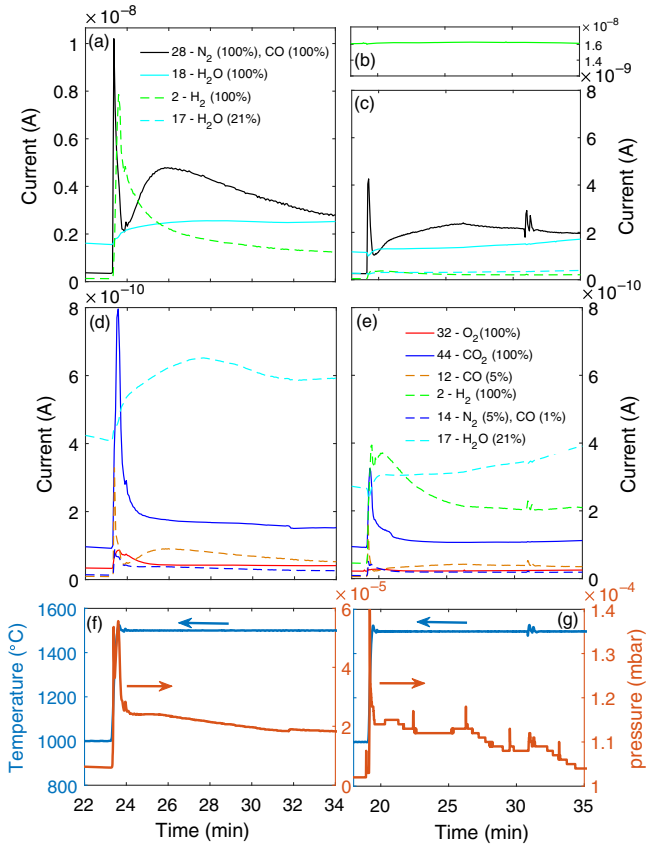

FIG. 4. The ion current for M/z ratios equal to 2, 12, 14, 17, 18, 28, 32, and 44 in the first 10 min of graphene growth at 1500 °C at (a),(d) high vacuum of 1 to 2×10^{-5} mbar and total pressure and temperature shown in (f). The M/z ion current is compared with low argon pressure growth at 1.1×10^{-4} mbar (9*N* purity) in (b), (c),(e), and the corresponding pressure and temperature time evolution is shown in (g).

The major identified reaction is a reaction of two major components in the furnace, carbon and water. We discuss this process in detail here. The epitaxial graphene can be grown quickly (2–5 min) at higher temperatures, or slowly (20–90 min) at lower temperatures. We find that 1430 °C for 20 min is equivalent to 1500 °C for 5 min in the amount of grown graphene. They are, however, not equivalent in the growth conditions concerning the growth environment. We discuss here the differences between the two regimes. The main issue is the content of water and carbon monoxide, as shown in Fig. 4 at the beginning of graphene growth. The water content is about 10%–15% for times shorter than 5 min, but it then grows steadily and completely dominates the growth atmosphere at times longer than 30 min. Detailed analysis of the growth ambient in high vacuum, Figs. 4(a), 4(d), and 4(f), shows a sharp total pressure rise accompanied by a sharp rise of ion current by 8×10^{-9} A at $M/z = 28$.

Similarly, the ion current increases at masses $M/z = 44$ by 0.6×10^{-9} A and $M/z = 12$ by 0.25×10^{-9} A. A significant rise of hydrogen—by the amount of 6×10^{-9} A—is also present. The water ion current is unchanged within the first 60 s of growth stage (III). A step rise of ion current is expected instead due to the step rise of temperature and the consequent step rise of mean velocity of the ions. The lack of such an ion step rise of water can be attributed to the reduction of the total amount of water in the chamber. The rise of $M/z = 28$ by 8×10^{-9} A is attributed to CO. The rise of CO is confirmed by the rise of ion current at $M/z = 12$ by 0.25×10^{-9} A, which is 3% (the expected CO contribution is 5%) of the major ion current rise at $M/z = 28$. The minor ion current peak at $M/z = 14$ of 0.05×10^{-9} A (0.6% of $M/z = 28$; the expected CO contribution is 1%) is also attributed to CO.

We conclude that there is no absolute change of nitrogen ($M/z = 28$, 14), and all content changes can be explained by increasing the amount of CO and adding a similar amount of hydrogen. The shift of the hydrogen peak towards longer times is caused by a slower pumping of hydrogen than of CO, water, or other heavier ions. The ion-current rise at mass $M/z = 44$ of 0.6×10^{-9} A is due to the carbon dioxide (CO_2). Therefore, the dynamics of the growth ambient is dominated by the chemical reaction

$$\mathrm{C}(s) + \mathrm{H_2O}(g) \rightleftharpoons \mathrm{CO}(g) + \mathrm{H_2}(g) + 7.5\%[\mathrm{CO_2}(g) + \mathrm{CH_4}]. \quad (1)$$

The major chemical reaction given by Eq. (1) is observed mainly on the short time scale below 30 s after each temperature step rise. The time scale between 30 and 100 s is dominated by pumping the products of Eq. (1) out of the furnace.

The long time scale above 2 min is dominated by both pumping of the residual gas and water outgassing from the stainless-steel furnace walls. This behavior is observed in both high-vacuum and low-pressure argon, and also in the case of a glassy graphite crucible in high vacuum, as shown in Fig. 3. The content changes only slowly for longer times (>60 s); however, water slowly becomes the dominant gas. The water source is at the surface of stainless-steel furnace walls. The main issue is that it can promote a reaction with carbon (1) even more, hence creating defects in a graphene layer. Therefore, it is preferential to grow graphene at higher temperatures for shorter times.

As the residual gas analysis has shown that it is more preferable to grow graphene at higher temperatures and shorter times, we grow single-layer graphene between 1500 °C and 1550 °C for 5 min in high vacuum, 5×10^{-6}–2×10^{-5} mbar. The 1500 °C for 5 min of growth seems to result in a patchy graphene with about 20%–40% of a buffer layer. The single-layer graphene is proven by Raman spectroscopy and discussed later. There are already signatures of bilayers at the higher temperature of 1550 °C for 5 min.

Growth in 800–1050 mbar of argon is approximately 30 °C–50 °C, shifted towards higher temperatures with

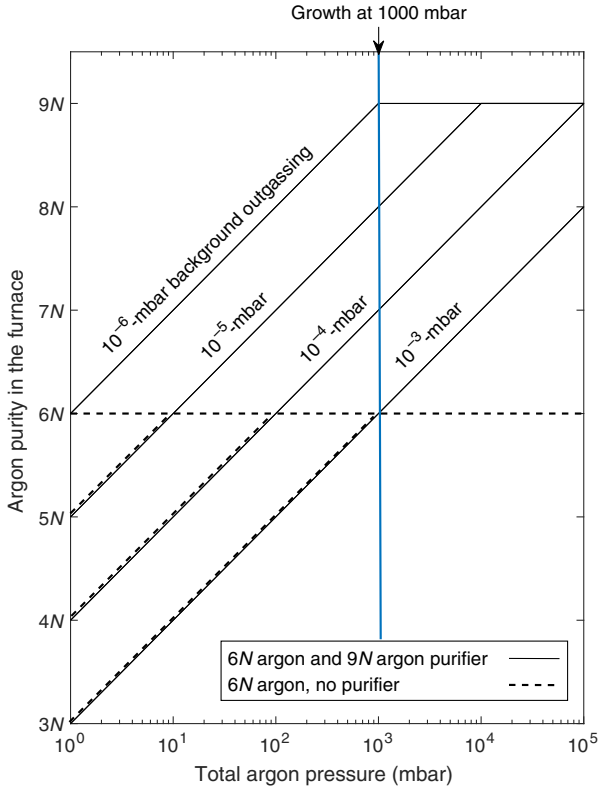

FIG. 5. A diagram of the growth environment purity as a function of total argon pressure in the furnace. The case of 6*N*-pure argon is plotted with dashed lines, and the case of 9*N* purity (purified from 6*N*) is plotted with solid lines. The final gas purity is calculated for four different background pressures, as shown by the labels 10^{-3} mbar, 10^{-4} mbar, 10^{-5} mbar, and 10^{-6} mbar in the diagram.

respect to growth in high vacuum. The buffer grows at about 1410 °C–1430 °C in high vacuum and at about 1450 °C at 800–1050 mbar of argon pressure. The growth is always done in the same graphite crucible with a hole 1 mm in diameter and 10 mm long. Argon acting on graphene growth is twofold. First, it is equivalent to the CCS method, where the lowered silicon sublimation is due to the small volume in a nearly closed graphite crucible. Second, argon pressure acts as an inhibitor for water outgassing, identified earlier as the major source of residual gas and a potential cause of defect formation in epitaxial graphene.

We note that high-purity argon is necessary in order to obtain an overall purity of growth conditions comparable to those in high vacuum at 1×10^{-5} mbar. An equivalent purity of argon gas for graphene growth at 1000 mbar is 8*N* (equal to 1000 mbar/10^{-5} mbar). A lower argon purity results in a higher relative content of residual gas, which leads to a higher total amount of, mainly, water at 1000 mbar of argon pressure growth [the total amount of water is discussed with respect to the total amount of water at high vacuum (10^{-5} mbar) growth].

Besides the gas purity, the background outgassing in the furnace also has to be taken into account. A typical water background pressure in an unbaked furnace is $10^{-6} - 10^{-5}$ mbar. If the background water pressure is higher, the overall argon purity in the furnace will be lower even with gas purifiers, as is described in Fig. 5. Figure 5 demonstrates the overall gas purity as a function of the total argon pressure for 2 degrees of argon purity. The solid (dashed) lines depict the total argon purity as a function of the total argon pressure for an inlet of 9*N*-(6*N*-) pure argon. The total gas purity cannot be higher than the inlet gas purity; therefore, all curves saturate at the value of inlet gas purity 9*N* (the solid lines) and 6*N* (the dashed lines). Figure 5 also shows the influence of four different background impurity pressures. The background impurity pressure is detrimental at low total argon pressures; therefore, it is expected that higher-quality graphene will be grown at higher argon pressures, as has been shown in the literature [12].

A further reduction of water outgassing could be done with a growth in argon flow. The graphene quality should be independent on the flow rate as long as the flow rate is much higher than the outgassing rate. Another important role of argon is the reduction of water and carbon reaction by a factor of 3 [as can be seen in Figs. 4(c), 4(e), and 4(g)] compared to the growth in high vacuum [Figures 4(a), 4(d), and 4(f)]. It can be assumed that the reaction rate will be reduced even further at higher argon pressure.

VI. SAMPLE CHARACTERIZATION

We compare six epitaxial-graphene samples grown in high vacuum (1550 °C for 5 min) at 10^{-5} mbar, in 9*N*-pure argon at 800 mbar (1600 °C for 5 min), in 6*N* argon at 800 mbar (1600 °C for 5 min), a sample grown in 9*N* argon and later annealed in high vacuum at 10^{-5} mbar for 5 min, a sample grown in 50-SLPH flow of 9*N* argon, and, finally, a sample that is first etched in 20 SLPH of 9*N* hydrogen at 1350 °C for 20 min and on which graphene is later grown in 50 SLPH of 9*N* argon at 1600 °C for 5 min. Each graphene growth time is 5 min. As the graphene Raman spectrum is merged with the SiC Raman spectrum, we decompose all spectra by non-negative matrix factorization (NMF), which we have described elsewhere [21].

We measure 3×3 μm^2 maps of Raman spectra with a step of 100 nm. Integration time is 2 s. We use a confocal microscope with a 100×-magnification microscope objective and numerical aperture NA = 0.9. The excitation laser wavelength is 532 nm, and the laser power on the sample surface is 5 mW. The measured spectra are organized into a matrix, and ten bare SiC spectra are added to facilitate removal of the SiC signal by NMF.

The Raman spectra are decomposed into three components for all samples. The first component is the SiC substrate, the second component is single-layer graphene, and the third component is bilayer graphene ribbons at the step edges, a buffer, or a mixture of a single layer and a bilayer. An example of a decomposed Ramana spectrum is shown in Fig. 6. The experimental data (the black curve) are

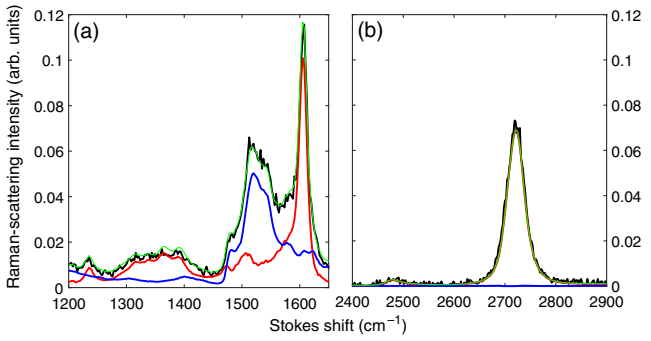

FIG. 6. An example of the measured Raman spectrum (the black curve) in the vicinity of (a) the D and G peak and (b) the $2D$ peak. The measured spectra are decomposed into the spectrum of SiC (the blue curve), graphene (the red curve), and the decomposed spectra are summed again (the green curve) to verify the quality of the decomposition.

compared with two NMF components (the blue and red curves), and these components are summed with the corresponding weights (the green curve) to verify the quality of the decomposition. The following analysis of Raman maps is performed selectively on the areas with a single layer. The number of graphene layers has been determined by several authors [22] from the ratio of the integrated $2D$ peak I_{2D} and the integrated G peak intensity I_G. This ratio is $\mathcal{N} = I_{2D}/I_G = 2$ for single-layer graphene, $\mathcal{N} = 1$ for a bilayer, and $\mathcal{N} < 1$ for more than two graphene layers.

We note that this relation is the most disputable, and it is valid only in the limit of a few graphene layers. It cannot be used, e.g., for determining the number of graphene layers of multilayer graphene on the C face of SiC. Our graphene samples are grown at about 50 °C above the lowest graphitization temperature for 5 min, and graphene is always grown on the Si face of SiC; therefore, we are in the limit of one to two layers, and this method can be used to determine the number of graphene layers. The narrow $2D$ peak [full width at half maximum (FWHM) below 40 cm^{-1}] is also a fingerprint of single-layer graphene [23]. The intensities, positions of peak maxima, and FWHMs of the D, G, and $2D$ peaks are summarized in Table I. The integrated intensities are calculated from the spectral intervals 1260–1450 cm^{-1} for the D peak, 1535–1650 cm^{-1} for the G peak, and 2600–2850 cm^{-1} for the $2D$ peak. The linear background is subtracted prior to integration.

We compare the single-layer graphene Raman spectra of all samples in Fig. 7. The spectrum energetically below the G peak consists of a three-component signal from the buffer (the peaks labeled B_1, B_2, B_3), as indicated by the magenta curve in Fig. 7(a), and it consists also of a series of narrow and weaker peaks, labeled D_1–D_7 in Fig. 7(a). Similar spectra have also been observed in epitaxial-graphene samples after subtracting the SiC background signal [24]. All peaks are related to the Raman signal from the 1-μm-thick surface layer in our confocal microscope. The peak D_2 at 1330 cm^{-1} can be attributed to the D peak in epitaxial graphene (carbon-carbon vibration in the nearest vicinity of the defect). The peaks D_2 and D_4 can be attributed to the carbon-carbon (C-C) vibration in the nearest-neighbor and next-nearest C-C pair neighbor of the defect site [25]. Peaks D_5, D_6, and D_7 can be related to the buffer layer. The origin of the D_1 peak is currently unknown. The ratio of the D-to-G peak integrated intensity cannot be determined due to the buffer-layer Raman signal.

The relative intensity of the three buffer-related peaks (B_1, B_2, and B_3) is different between the samples with a buffer only and samples with single-layer graphene (graphene and buffer), as can be seen in Fig. 7. For this reason, it is not possible to simply subtract the buffer-layer signal from the graphene signal. Hence, we compare the quality of different graphene samples by examining the $2D$ peak-position distribution and the FWHM of the $2D$ peak. The $2D$ peak position corresponds to mechanical strain and the FWHM has been correlated to the graphene quality by other authors [26]. The statistical distribution of the $2D$ peak position is shown in Fig. 8.

The first three samples show small differences in the mean $2D$ peak position and its variance. However, the reannealed sample, Fig. 8(d) shows an inhomogeneous distribution of the $2D$ peak position. This distribution shows on large variations of strain across the sample. We determine the mechanical strain ϵ,

$$\epsilon = \frac{\omega_{2D} - \omega_{2D,0}}{2\omega_{2D,0}\gamma_{2D}}, \tag{2}$$

TABLE I. The integrated intensities I_{2D}, I_G, and I_D, the peak positions ω_{2D}, ω_G, and ω_D, and the spectral widths FWHM_{2D}, FWHM_G and FWHM_D of the $2D$, G, and D peaks.

Sample	I_{2D} (arb. units)	ω_{2D} (cm^{-1})	FWHM_{2D} (cm^{-1})	I_G (arb. units)	ω_G (cm^{-1})	FWHM_G (cm^{-1})	I_D (arb. units)	ω_D (cm^{-1})	FWHM_D (cm^{-1})	ϵ (%)
Ar 9N	13.8	2706.1	33.6	8.3	1595.4	12.1	4.0	1356.2	85.1	0.19
vacuum	12.7	2708.3	35.7	9.5	1600.3	17.0	5.2	1356.2	90.2	0.21
Ar 6N	13.2	2710.5	35.7	8.0	1602.9	14.6	4.3	1358.8	92.7	0.22
Ar 9N + vacuum	15.6	2700.0	39.9	9.0	1598.0	19.4	3.6	1351.3	92.7	0.15–0.33
Ar 9N, flow	12.5	2723.1	35.6	8.0	1607.7	14.6	4.8	1368.9	70.1	0.31
H_2 + Ar 9N, flow	14.7	2701.9	29.4	7.1	1590.5	14.6	3.2	1351.2	52.7	0.17

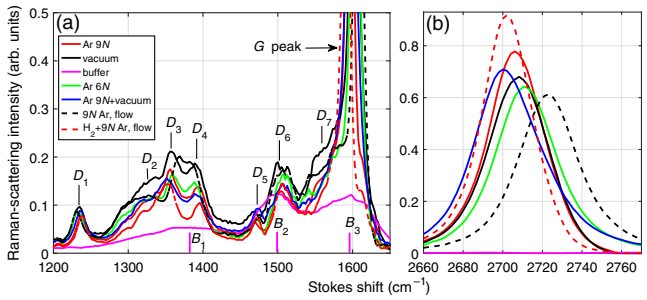

FIG. 7. Comparison of the decomposed spectra related to the graphene in the vicinity of the (a) D and G peak and (b) $2D$ peak. The four methods of epitaxial-graphene growth are compared. Growth in $9N$ argon at 800 mbar (the red curve), growth in high vacuum (the black curve), growth in $6N$ argon (the green curve), and growth in $9N$ argon with a subsequent annealing in high vacuum (the blue curve). All spectra are normalized by the maximal value of the G peak.

given by the measured position of the $2D$ peak ω_{2D}, the position of the $2D$ peak at zero strain $\omega_{2D,0} = 2677\ \mathrm{cm}^{-1}$, and the Grüneisen parameter for the $2D$ peak $\gamma_{2D} = 2.8$ [27]. The effects of charge density on the position of the $2D$ peak are negligible [28]. Strain spans $\epsilon = 0.15\%$–0.33%, depending on growth conditions, as can be seen in Table I. The expected strain $\epsilon_{\mathrm{theory}} = (13a_{0,G} - 6\sqrt{3}a_{0,\mathrm{SiC}}/13a_{0,G}) = 0.19\%$ is determined from graphene ($a_{0,G} = 2.462$ Å) [29] and SiC ($a_{0,\mathrm{SiC}} = 3.073$ Å) lattice constants at 300 K assuming a $6\sqrt{3} \times 6\sqrt{3}R30°$ SiC-graphene supercell [30] containing 13 graphene unit cells and a mutual rotation of the graphene and SiC lattices by 30°. The expected strain is observed in samples grown in $9N$ argon. Samples grown in high vacuum or $6N$ argon show higher strain (0.21% to 0.22%). The reannealed sample shows a wide distribution of strain ranging from 0.15% to 0.33%.

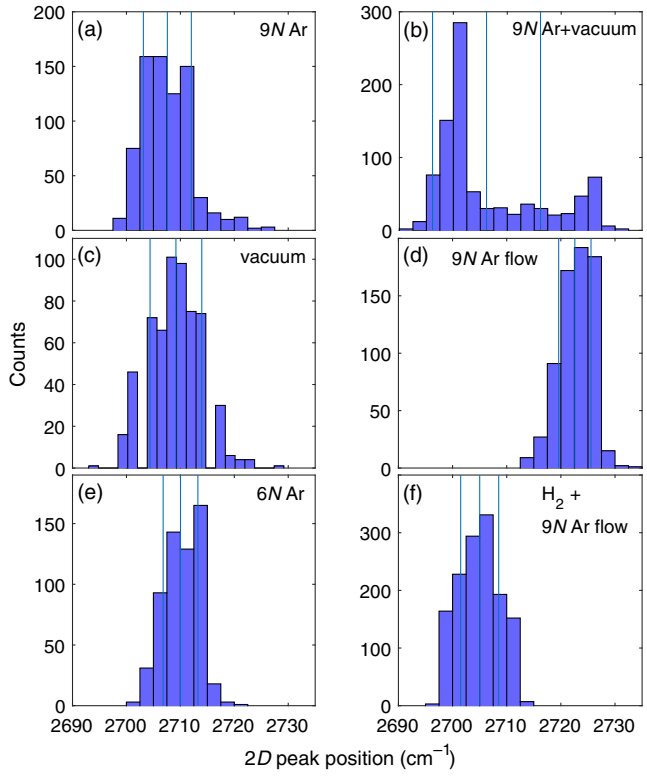

FIG. 8. Statistics of the $2D$ peak position of graphene grown by four different methods. (a) Growth in static ambient of $9N$ argon at 1000 mbar. (b) Growth in static ambient of $9N$ argon with a subsequent annealing in high vacuum. (c) Growth in high vacuum. (d) Growth in 50 SLPH of $9N$ argon at 1000 mbar. (e) Growth in static ambient of $6N$ argon. (f) Samples etched in 20 SLPH of $9N$ hydrogen prior to growth and graphene was grown in 50 SLPH of $9N$ argon.

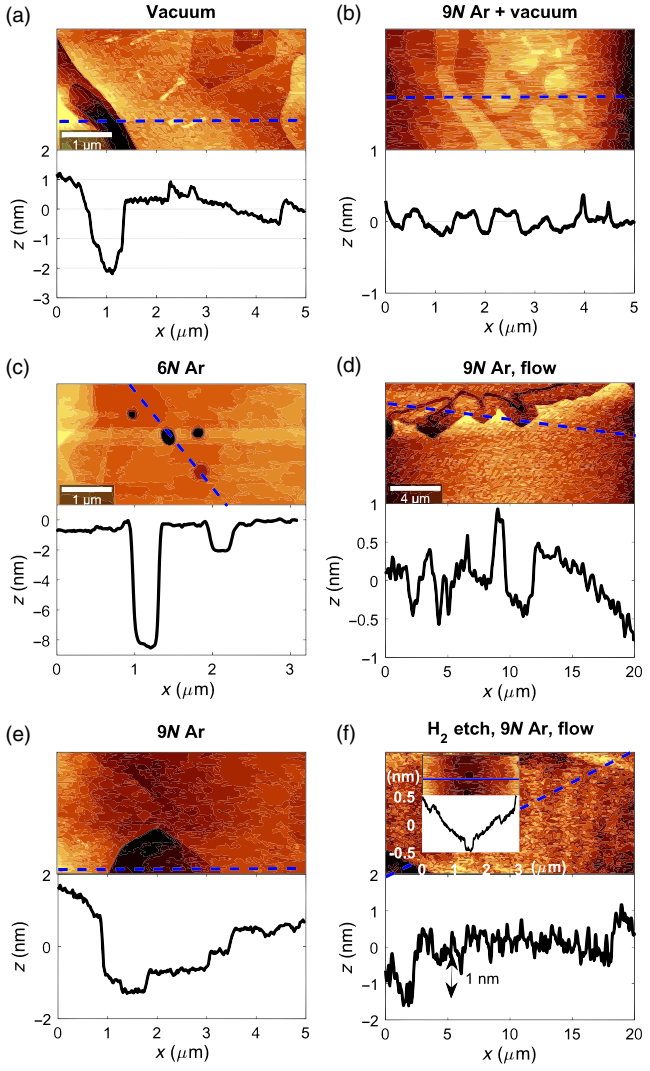

FIG. 9. Atomic force microscopy of graphene grown in (a) high vacuum, (b) $9N$ argon with additional annealing in high vacuum, (c) $6N$ argon, (d) 50 SLPH of $9N$ argon, (e) static ambient of $9N$ argon, and (f) Samples etched in 20 SLPH of $9N$ hydrogen prior to growth and graphene was grown in 50 SLPH of $9N$ argon. Height profiles are shown below each AFM image, and the positions of the profile cuts are marked by blue dashed lines. The inset in (f) displays an enlargement of the wide terrace.

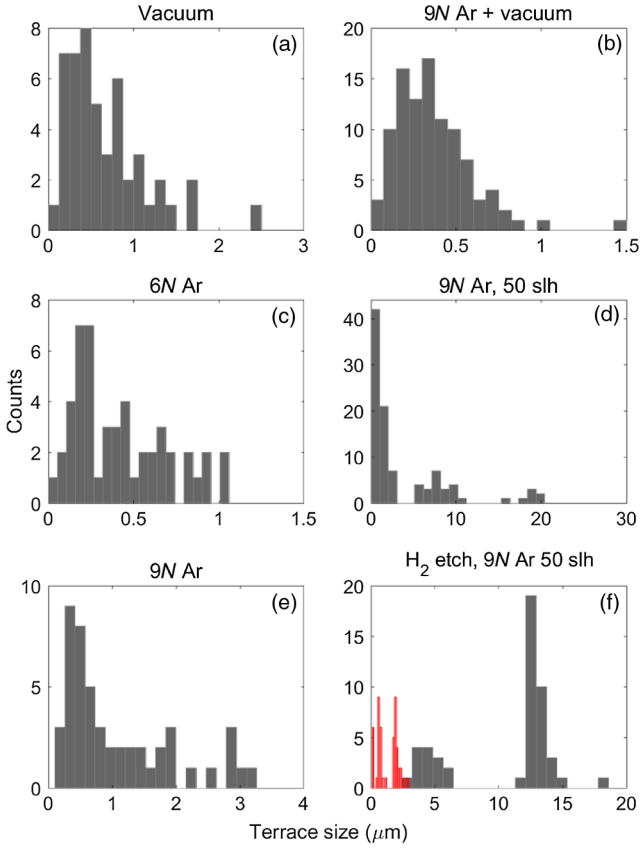

FIG. 10. Histograms of the terrace sizes in samples grown in (a) high vacuum, (b) 9*N* argon with additional annealing in high vacuum, (c) 6*N* argon, (d) 50 SLPH of 9*N* argon, (e) a static ambient of 9*N* argon, and (f) H_2 etched samples (20 SLPH of hydrogen) and graphene grown in 50 SLPH of 9*N* argon. The histograms in (f) show distributions of both large and 1-nm-high terraces (the black histogram) and 2.5-Å shallow terraces (the red histogram).

The graphene grown in 50 SLPH of 9*N* argon, however, shows high uniform strain of about 0.31%. The most relaxed strain is observed in graphene grown on a hydrogen-etched sample and subsequently grown in 50 SLPH of 9*N* argon.

We measure AFM in a contact mode using a cantilever with a stiffness of 0.5 N/m. The results are summarized in Fig. 9, where the typical morphology of all samples is shown after graphene growth. The height profiles are also shown along selected lines. The samples grown in high vacuum exhibit a small size of SiC terraces below 1 μm, and the step height is below 2 nm. Similar terrace sizes are observed after growth in 6*N* argon. Here, we observe (1.5–8)-nm-deep pits. The terrace size is increased locally up to 2 μm when graphene is grown in 9*N* argon and the step height is between 2.5 Å and 2 nm. The step height of 2.5 Å corresponds to the height of the SiC bilayer (which comprises one layer of carbon and one layer of silicon).

We demonstrate the effect of SiC etching by residual gas (with mainly water as the dominant residual gas) in the sample grown first in 9*N* argon and later reannealed in high vacuum. The grain size is again reduced below 1 μm, which is comparable to the terrace size in vacuum-grown graphene. Pit formation is not observed in this sample. The widest terraces in the range of 5 to 20 μm is observed in the samples grown in 50-SLPH flow of 9*N* argon, where the step height is below 1 nm.

We reach the most regular surface when samples are hydrogen etched prior to the growth in 50 SLPH of 9*N* argon. The wide terraces are accompanied by two types of steps. The steps at the edge of wide terraces are 1 nm high, which corresponds to four SiC bilayers, each being 2.5 Å high. We note that we use 4*H*-SiC. The second kind of step is found occasionally within a large terrace. These steps are 2.5 Å high; see the inset of Fig. 9(f). The statistics of all observed terrace sizes are shown in the histograms in Fig. 10.

We measure the Hall effect to determine charge density and carrier mobility. The room-temperature measurements are performed in a magnetic field of up to ± 0.35 T in the van der Pauw configuration. A dc source is used ($I = 1$ μA), and all combinations of current directions and voltages are measured to determine the specific resistance and Hall coefficient. Typical transport coefficients are shown in Table II.

TABLE II. Transport properties of epitaxial graphene grown in high vacuum, $5 \times 10^{-6} - 10^{-5}$ mbar; an 800-mbar, 6*N*-argon atmosphere; an 800-mbar, 9*N*-argon atmosphere; and an 800-mbar, 9*N*-argon atmosphere, with subsequent annealing in vacuum, in 50 SLPH of 9*N* argon and in 50 SLPH of 9*N* argon with prior etching in H_2. The typical values are presented for specific two-dimensional resistivity (resistance per square) $R_\square$, Hall coefficient R_H, apparent carrier density $1/eR_H$, and apparent carrier mobility $R_H/R_\square$.

	$R_\square$ ($\Omega/\square$)	R_H (Ω/T)	$1/eR_H$ (10^{12} cm^{-2})	$R_H/R_\square$ (cm^2 V^{-1} s^{-1})
high vacuum	2400 ± 100	-96 ± 4	-6.5 ± 0.5	390 ± 20
6*N* Ar	6970 ± 200	-31 ± 5	-2.0 ± 0.3	44 ± 7
9*N* Ar, no flow	1150 ± 50	-78 ± 10	-8.0 ± 1.0	690 ± 80
9*N* Ar, no flow, annealed in vacuum	2920 ± 150	-240 ± 30	-2.6 ± 0.3	820 ± 100
9*N* Ar, 50 SLPH	2150 ± 100	-168 ± 15	-3.7 ± 0.3	780 ± 80
9*N* Ar, 50 SLPH, H_2 etching	3510 ± 180	-340 ± 40	-1.8 ± 0.2	980 ± 120

We observe 2×-lower specific resistance and 1.8×-higher apparent carrier mobility in argon-grown graphene. A further increase of carrier mobility from 690 ± 80 to 780 ± 80 $cm^2\,V^{-1}\,s^{-1}$ is reached in 50 SLPH of 9*N* argon. If the SiC wafer is etched in hydrogen ($5\%H_2/95\%Ar$ at 1000 mbar, 1700°C for 5 min) prior to growth in 50-SLPH 9*N* argon, the mobility increases by 25% to 980 $cm^2\,V^{-1}\,s^{-1}$. The 9*N*-argon-grown sample annealed later in vacuum shows higher mobility than the graphene grown only in 9*N* argon. This result is partially in contradiction with smaller SiC terraces measured by AFM. The reason for higher mobility lies in the inequivalent growth conditions.

The annealing in vacuum is performed at 1550 °C for 5 min. It is necessary to keep the same etching rate of SiC by residual water as in the case of growth in vacuum only. However, since 1550 °C for 5 min is a graphene growth temperature in vacuum and graphene is already present on the sample after the growth in 9*N* argon, we observe two effects after annealing. First, the residual water etches SiC and forms small crystallographic terraces. Second, the single-layer graphene becomes overgrown, thus forming larger areas with bilayer graphene, as can be noticed in a Raman spectrum as a broader 2*D* peak [Table I]. We note that all samples show a small negative Hall coefficient R_H ranging from −31 to −168 Ω/T, indicating *n*-type doping on the order of 10^{12} cm^{-2}.

VII. DISCUSSION

The results of Raman scattering, AFM, and Hall-effect measurements show that graphene grown in ultrapure argon at 800 mbar is of higher quality than graphene grown in high vacuum or 6*N* argon. The growth in high vacuum or 6*N* argon leads to smaller SiC terraces, even if the growth conditions are well optimized by high-temperature bakeout of all three major parts of the graphene furnace (gas inlet pipes, main body of the furnace and graphite crucible). A key issue in graphene growth is the presence of water and water outgassing from stainless-steel surfaces. We observe a chemical reaction of water and solid-state carbon at all stages of graphene growth. This reaction is important within the first minute of each graphene growth step. It becomes important again when graphene is grown for times greater than 20–30 min. This water desorption is caused by the gradual furnace warm-up and the consequent water outgassing from previously colder furnace parts.

As we do not know the origin of carbon, we assume that the main source is a graphite crucible for a time scale below 60 s at the beginning of each growth step. However, as graphene grows, the carbon source can be also graphene itself. The experimental proof of such reaction with graphene requires us to distinguish between a reaction of carbon with water and an etching of SiC. The SiC wafer can be etched by water [31],

$$\mathrm{SiC} + 3\mathrm{H_2O}(g) \rightarrow \mathrm{SiO_2} + \mathrm{CO}(g) + 3\mathrm{H_2}(g), \quad (3)$$

at T > 1127 °C. The reaction of residual water with SiC in high vacuum has been extensively studied [31] and it is now well established that this reaction leads to a rough SiC surface. SiC can also react with carbon monoxide [32],

$$\mathrm{SiC} + \mathrm{CO}(g) \rightarrow \mathrm{SiO}(g) + 2\mathrm{C}(s), \quad (4)$$

or hydrogen [33],

$$\mathrm{SiC} + 4\mathrm{H_2} \rightarrow \mathrm{SiH_4} + \mathrm{CH_4}, \quad (5)$$

at the ideal crystal-lattice sites, or it can react as

$$2\mathrm{SiC} + 5\mathrm{H_2} \rightarrow 2\mathrm{SiH_4} + \mathrm{C_2H_2}, \quad (6)$$

at lattice defects.

As our measurements indicate, the content of CO, H_2O, and H_2 varies within 10%–20% in high vacuum and the content of hydrogen is reduced to 1% in argon, while the content of $CO(g)$ and H_2O is lowered to 10% or below. The lowered amount of residual gases in ambient argon correlates with better SiC surface morphology. The high-vacuum-grown samples exhibit smaller SiC terrace widths below 1 μm and irregular meandering. We reach wider SiC steps up to 2 μm in 9*N* argon, and the step width increases to 20 μm when we grow graphene in a 50-SLPH flow of 9*N* argon. Therefore, we assume that reaction of residual gas with either SiC or graphene can be a reason for lower sample quality.

We note that the sensitivity of our RGA does not allow us to observe the amount of a residual gas which is expected to be observed in any reaction where a SiC wafer of the size $3.5 \times 3.5 \times 0.5$ mm^3 is involved. The reactions with a graphite crucible provide much higher amounts of gaseous product because of its larger volume and larger geometrical area, and also due to the porosity of graphite, which greatly increases the effective surface area. For this reason, we are currently unable to determine which of the above-discussed reactions with SiC or graphene is dominant.

However, we can conclude that, based on the content of residual gas, it is preferable to grow graphene at rather high temperatures and short times in order to reduce the amount of time that SiC or graphene is irregularly etched. A disadvantage of a short growth time is that there is no temporally stable growth-atmosphere content. Moreover, it differs slightly from one sample to another. Both hydrogen and carbon monoxide are produced in a reaction of carbon and water; hence, the reduction of water seems to be a good candidate for improving SiC step formation. Hydrogen is also present as a residual gas in high-vacuum furnaces. An uncontrolled content of water and hydrogen is therefore undesirable during graphene growth.

The growth in argon is shown to lead to more stable growth-atmosphere content, with a small rate of carbon and

water reactions and also a smaller amount of residual gases (CO, H_2O, and H_2) capable of etching SiC. The high argon pressure reduces both the water outgassing and the mean free path of water molecules. The shorter mean free path can be used to restrict water transport towards grown graphene when growth is performed in argon flow, as we demonstrate experimentally through SiC atomically flat terraces in the range of 3–20 μm. Argon acts as a carrier gas when growth is performed in a nonstatic ambient. The flow rate is not supposed to improve the overall amount of residual gas because the residual gas is homogeneously spread within the furnace volume. However, argon carrier gas continuously removes any remaining outgassed water, and it also removes products of any remaining reactions of the residual gas with a graphite crucible, a SiC wafer, or graphene. We also point out that it is essential to use ultrapure argon (8*N* or 9*N*) at the furnace inlet. A common 6*N* argon at 1000 mbar is, in terms of the total amount of residual gas, equivalent to vacuum growth at 10^{-3} mbar (if background outgassing leads to lower or equal pressure). Therefore, growth in 6*N* argon at 1000 mbar will lead to smaller SiC terraces than are found in vacuum-grown samples, as we demonstrate experimentally by AFM in this work.

Air permeability of graphite brings constrictions on a crucible storage. The nitrogen and water is absorbed into the crucible after a longer exposure to air. It is, therefore, suggested to store ISP graphite in vacuum or in an inert gas. Glassy graphite is impermeable to air components; however, the surface absorbants still lead to higher desorption when a glassy graphite crucible is heated to growth temperatures.

Raman spectroscopy has proven to be a versatile tool to determine most of the basic graphene properties, such as mechanical strain and the number of graphene layers. The relative strength of the SiC Raman spectrum and the intensity of the graphene spectrum (particularly the intensity of the *G* peak) has been used to determine the number of graphene layers by certain authors [34]. We point out that this method can be calibrated (intensity ratio to the number of layers) to only a given experimental setup, and it is not transferable. The reason for this limitation is mainly due to different microscope objective numerical apertures (NAs). We demonstrate the effect of a numerical aperture in Fig. 11.

The small NA objectives probe the signal deeper into bulk crystal, even if it is focused properly on a surface graphene layer. As a result, the relative intensity of graphene to the SiC bulk spectrum will be smaller than the ratio determined from Raman spectra measured with a high-NA objective. A similar issue comes up in a grain-size determination from the ratio of *D*-to-*G* peak intensity. If a low-NA objective is used (the green curve in Fig. 11), the graphene signal is weak relative to the SiC signal and the *D* peak can seem to be negligible with respect to the SiC [35]. The small *D* peak is then mistakenly identified as a signature of high-quality graphene.

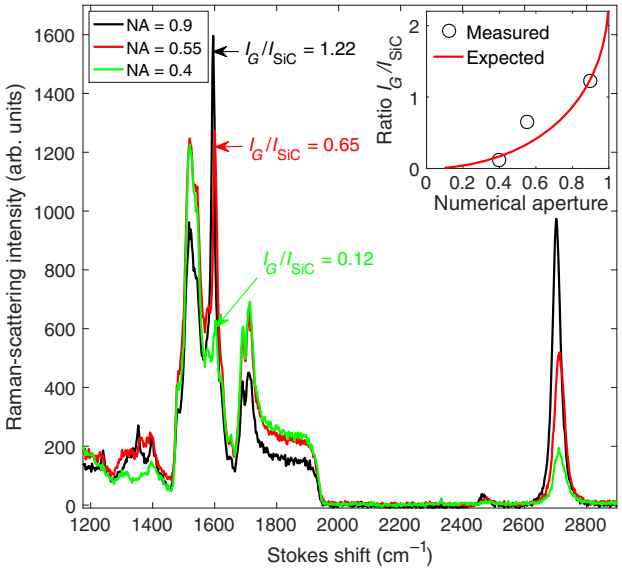

FIG. 11. Raman spectra measured by three microscope objectives with numerical apertures 0.4, 0.55, and 0.9. (Inset) Ratio of the Raman signal to graphene and SiC measured (circles) by microscope objectives with numerical apertures 0.4, 0.55, and 0.9. The measured ratios $R = I_G/I_{SiC}$ are compared with the expected trend (the solid red curve) given by Eq. (8).

The quantitative estimate of the ratio of the Raman signal from graphene I_G and SiC I_{SiC} can be made assuming a Gaussian laser beam focused by microscope objective, and also assuming a confocal microscope setup. The volume of the sample excited by a laser beam and probed by a confocal microscope is

$$V = \int_0^{z_0} \int_0^{W(z)} \int_0^{2\pi} r dr d\varphi dz, \tag{7}$$

where the z axis is chosen along the laser beam, we assume there is a focused microscope objective (the sample at $z = 0$), $W(z)$ is the z-dependent width of the Gaussian beam, r and φ are the radial distance and the angle of the cylindrical coordinate system, and we integrate only over the confocal depth ($z = 0$ to z_0, z_0 is the Rayleigh parameter of the Gaussian beam). The excited and probed volume is then $V = \frac{4}{3}\pi W_0^2 z_0$ (W_0 is a half-width of the Gaussian beam waist). The probed volume of the graphene layer is $V_G = \pi W_0^2 t$, where t is the graphene thickness. The half-width of the Gaussian beam W_0 can be related to the numerical aperture of the objective NA by $W_0 = \lambda/[\pi \arcsin(\mathrm{NA})]$, where λ is the wavelength of the excitation laser. The ratio of the graphene-to-SiC signals $R = I_G/I_{SiC} = t/z_0$ and, using the relation $z_0 = \pi W_0^2/\lambda$, we get

$$\frac{I_G}{I_{SiC}} = \frac{\pi t}{\lambda} \arcsin^2(\mathrm{NA}). \tag{8}$$

The relative intensity of the Raman signal from graphene increases when a higher NA objective is used. This effect is also demonstrated in Fig. 11.

We use three objectives, with NAs 0.4, 0.55, and 0.9, and measure Raman spectra from one spot on the sample. The ratio $R = I_G/I_{SiC}$ follows the expected trend given by Eq. (8); see the inset in Fig. 11. The measured scaling does not follow exactly the dependence $\arcsin^2 \mathrm{NA}$ due to factors not included in our simple estimate as abberations of the objective or the aperture diameter of the confocal microscope. The small shifts of the G and $2D$ peaks can be caused by a slightly different position on the sample and also by a differing laser spot size, which scales also with the NA.

VIII. CONCLUSION

In this paper, we analyze experimentally the graphene growth environment and its influence on graphene quality. Residual gas analysis shows the important role of a water reaction with carbon in a high-vacuum growth ambient. We explore the reduced role of the residual gas in 9N-pure argon and we compare high-vacuum and argon-grown graphene. The gas purity and the gas flow are shown to be detrimental factors for high-quality graphene for electronic applications. The mechanical strain, the strain lateral distribution, and the number of graphene layers is determined from Raman-spectroscopy mapping. The SiC morphology is measured by AFM and the electronic quality of grown graphene is confirmed by Hall-effect measurements in the van der Pauw configuration. Raman-scattering spectroscopy, AFM, and Hall-effect measurements proof that the highest graphene quality is grown in a flow of high-purity argon due to the reduced rates of residual gas reactions.

ACKNOWLEDGMENTS

Financial support from the Grant Agency of the Czech Republic under Contract No. 16-15763Y is gratefully acknowledged. Raman spectroscopy has been measured as part of Project No. VaVpI CZ.1.05/4.1.00/16.0340. We acknowledge the technical support from K. Uhlířová and the fruitful discussion with P. Hlídek and R. Grill.

[1] C. Berger, Z. M. Song, T. B. Li, X. B. Li, A. Y. Ogbazghi, R. Feng, Z. T. Dai, A. N. Marchenkov, E. H. Conrad, P. N. First, and W. A. de Heer, Ultrathin epitaxial graphite: 2d electron gas properties and a route toward graphene-based nanoelectronics, J. Phys. Chem. B **108**, 19912 (2004).

[2] Jan Kunc, Yike Hu, James Palmer, Zelei Guo, John Hankinson, Salah H. Gamal, Claire Berger, and Walt A. de Heer, Planar edge Schottky barrier-tunneling transistors using epitaxial graphene/SiC junctions, Nano Lett. **14**, 5170 (2014).

[3] Rui Dong, Zelei Guo, James Palmer, Yike Hu, Ming Ruan, John Hankinson, Jan Kunc, Swapan K. Bhattacharya, Claire Berger, and Walt A. de Heer, Wafer bonding solution to epitaxial graphene-silicon integration, J. Phys. D **47**, 094001 (2014).

[4] Gholam Reza Yazdi, Tihomir Iakimov, and Rositsa Yakimova, Epitaxial graphene on SiC: A review of growth and characterization, Crystals **6**, 53 (2016).

[5] Lydia Nemec, Florian Lazarevic, Patrick Rinke, Matthias Scheffler, and Volker Blum, Why graphene growth is very different on the C face than on the Si face of SiC: Insights from surface equilibria and the $(3\times3)-3C-\mathrm{SiC}(\bar{1}\,\bar{1}\,\bar{1})$ reconstruction, Phys. Rev. B **91**, 161408(R) (2015).

[6] Masato Inoue, Hiroyuki Kageshima, Yoshihiro Kangawa, and Koichi Kakimoto, First-principles calculation of 0th-layer graphene-like growth of C on SiC(0001), Phys. Rev. B **86**, 085417 (2012).

[7] Hiroyuki Kageshima, Hiroki Hibino, Hiroshi Yamaguchi, and Masao Nagase, Stability and reactivity of steps in the initial stage of graphene growth on the SiC(0001) surface, Phys. Rev. B **88**, 235405 (2013).

[8] J. Borysiuk, J. Sołtys, R. Bożek, J. Piechota, S. Krukowski, W. Strupiński, J. M. Baranowski, and R. Stępniewski, Role of structure of C-terminated 4H-SiC$(000\bar{1})$ surface in growth of graphene layers: Transmission electron microscopy and density functional theory studies, Phys. Rev. B **85**, 045426 (2012).

[9] G. F. Sun, Y. Liu, S. H. Rhim, J. F. Jia, Q. K. Xue, M. Weinert, and L. Li, Si diffusion path for pit-free graphene growth on SiC(0001), Phys. Rev. B **84**, 195455 (2011).

[10] M. Ostler, I. Deretzis, S. Mammadov, F. Giannazzo, G. Nicotra, C. Spinella, Th. Seyller, and A. La Magna, Direct growth of quasi-free-standing epitaxial graphene on nonpolar SiC surfaces, Phys. Rev. B **88**, 085408 (2013).

[11] Taisuke Ohta, N. C. Bartelt, Shu Nie, Konrad Thürmer, and G. L. Kellogg, Role of carbon surface diffusion on the growth of epitaxial graphene on SiC, Phys. Rev. B **81**, 121411(R) (2010).

[12] M. L. Bolen, T. Shen, J. J. Gu, R. Colby, E. A. Stach, P. D. Ye, and M. A. Capano, Empirical study of Hall bars on few-layer graphene on C-face 4H-SiC, J. Electron. Mater. **39**, 2696 (2010).

[13] Mattias Kruskopf, Davood Momeni Pakdehi, Klaus Pierz, Stefan Wundrack, Rainer Stosch, Thorsten Dziomba, Martin Goetz, Jens Baringhaus, Johannes Aprojanz, Christoph Tegenkamp, Jakob Lidzba, Thomas Seyller, Frank Hohls, Franz J. Ahlers, and Hans W. Schumacher, Comeback of epitaxial graphene for electronics: Large-area growth of bilayer-free graphene on SiC, 2D Mater. **3**, 041002 (2016).

[14] James Palmer, Jan Kunc, Yike Hu, John Hankinson, Zelei Guo, Claire Berger, and Walt A. de Heer, Controlled epitaxial graphene growth within removable amorphous carbon corrals, Appl. Phys. Lett. **105**, 023106 (2014).

[15] J. Hass, W. A. de Heer, and E. H. Conrad, The growth and morphology of epitaxial multilayer graphene, J. Phys. Condens. Matter **20**, 323202 (2008).

[16] Weijie Lu, Roland Barbosa, Edwina Clarke, Kurt Eyink, Lawrence Grazulis, William C. Mitchel, and John J. Boeckl, Interface oxidative structural transitions in graphene growth on SiC (0001), J. Phys. Chem. C **116**, 15342 (2012).

[17] Weijie Lu, John J. Boeckl, and William C. Mitchel, A critical review of growth of low-dimensional carbon nanostructures on SiC (0 0 0 1): Impact of growth environment, J. Phys. D **43**, 374004 (2010).

[18] Jinsung Kwak, Tae-Yang Kwon, Jae Hwan Chu, Jae-Kyung Choi, Mi-Sun Lee, Sung Youb Kim, Hyung-Joon Shin, Kibog Park, Jang-Ung Park, and Soon-Yong Kwon, In situ observations of gas phase dynamics during graphene growth using solid-state carbon sources, Phys. Chem. Chem. Phys. **15**, 10446 (2013).

[19] Sebastian W. Pattinson, Vinay Ranganathan, Hajime K. Murakami, Krzysztof K. K. Koziol, and Alan H. Windle, Nitrogen-induced catalyst restructuring for epitaxial growth of multiwalled carbon nanotubes, ACS Nano **6**, 7723 (2012).

[20] Walt A. de Heer, Claire Berger, Ming Ruan, Mike Sprinkle, Xuebin Li, Yike Hu, Baiqian Zhang, John Hankinson, and Edward Conrad, Large area and structured epitaxial graphene produced by confinement controlled sublimation of silicon carbide, Proc. Natl. Acad. Sci. U.S.A. **108**, 16900 (2011).

[21] J. Kunc, Y. Hu, J. Palmer, C. Berger, and W. A. de Heer, A method to extract pure Raman spectrum of epitaxial graphene on SiC, Appl. Phys. Lett. **103**, 201911 (2013).

[22] Jih-Shang Hwang, Yu-Hsiang Lin, Jeong-Yuan Hwang, Railing Chang, Surojit Chattopadhyay, Chang-Jiang Chen, Peilin Chen, Hai-Pang Chiang, Tsong-Ru Tsai, Li-Chyong Chen, and Kuei-Hsien Chen, Imaging layer number and stacking order through formulating Raman fingerprints obtained from hexagonal single crystals of few layer graphene, Nanotechnology **24**, 015702 (2013).

[23] Dong Su Lee, Christian Riedl, Benjamin Krauss, Klaus von Klitzing, Ulrich Starke, and Jurgen H. Smet, Raman spectra of epitaxial graphene on SiC and of epitaxial graphene transferred to SiO_2, Nano Lett. **8**, 4320 (2008).

[24] Kevin M. Daniels, M. Mehdi Jadidi, Andrei B. Sushkov, Anindya Nath, Anthony K. Boyd, Karthik Sridhara, H. Dennis Drew, Thomas E. Murphy, Rachael L. Myers-Ward, and D. Kurt Gaskill, Narrow plasmon resonances enabled by quasi-freestanding bilayer epitaxial graphene, 2D Mater. **4**, 025034 (2017).

[25] Philipp Vecera, Julio C. Chacon-Torres, Thomas Pichler, Stephanie Reich, Himadri R. Soni, Andreas Goerling, Konstantin Edelthalhammer, Herwig Peterlik, Frank Hauke, and Andreas Hirsch, Precise determination of graphene functionalization by in situ Raman spectroscopy, Nat. Commun. **8**, 15192 (2017).

[26] Joshua A. Robinson, Maxwell Wetherington, Joseph L. Tedesco, Paul M. Campbell, Xiaojun Weng, Joseph Stitt, Mark A. Fanton, Eric Frantz, David Snyder, Brenda L. VanMil, Glenn G. Jernigan, Rachael L. Myers-Ward, Charles R. Eddy, Jr., and D. Kurt Gaskill, Correlating Raman spectral signatures with carrier mobility in epitaxial graphene: A guide to achieving high mobility on the wafer scale, Nano Lett. **9**, 2873 (2009).

[27] Diedrich A. Schmidt, Taisuke Ohta, and Thomas E. Beechem, Strain and charge carrier coupling in epitaxial graphene, Phys. Rev. B **84**, 235422 (2011).

[28] C. Stampfer, F. Molitor, D. Graf, K. Ensslin, A. Jungen, C. Hierold, and L. Wirtz, Raman imaging of doping domains in graphene on SiO_2, Appl. Phys. Lett. **91**, 241907 (2007).

[29] Monica Pozzo, Dario Alfè, Paolo Lacovig, Philip Hofmann, Silvano Lizzit, and Alessandro Baraldi, Thermal Expansion of Supported and Freestanding Graphene: Lattice Constant versus Interatomic Distance, Phys. Rev. Lett. **106**, 135501 (2011).

[30] K. V. Emtsev, F. Speck, Th. Seyller, L. Ley, and J. D. Riley, Interaction, growth, and ordering of epitaxial graphene on SiC{0001} surfaces: A comparative photoelectron spectroscopy study, Phys. Rev. B **77**, 155303 (2008).

[31] E. J. Opila, Variation of the oxidation rate of silicon carbide with water-vapor pressure, J. Am. Ceram. Soc. **82**, 625 (1999).

[32] D. P. Butt, R. E. Tressler, and K. E. Spear, Corrosion of SiC materials in N_2-H_2-CO gaseous environments: I. Thermodynamics and kinetics of reactions, J. Am. Ceram. Soc. **75**, 3257 (1992).

[33] Y. Kim and D. R. Olander, Reaction of β-SiC with thermal atomic-hydrogen by modulated molecular-beam mass-spectrometry, Surf. Sci. **313**, 399 (1994).

[34] Shriram Shivaraman, M. V. S. Chandrashekhar, John J. Boeckl, and Michael G. Spencer, Thickness estimation of epitaxial graphene on SiC using attenuation of substrate Raman intensity, J. Electron. Mater. **38**, 725 (2009).

[35] Dong Su Lee, Christian Riedl, Benjamin Krauss, Klaus von Klitzing, Ulrich Starke, and Jurgen H. Smet, Raman spectra of epitaxial graphene on SiC and of epitaxial graphene transferred to SiO_2, Nano Lett. **8**, 4320 (2008).